Mechanism of deformation around northern Hejin, China, observed by InSAR

Ji Lingyun[1], Liu Liwei[1], Li Ning[1], Liu Ruichun[2] and Zhou Cong[1]

[1] *Second Crust Monitoring and Application Center, China Earthquake Administration, Xi'an 710054, China*

[2] *Earthquake Administration of Shanxi Province, China Earthquake Administration, Taiyuan 030021, China*

Abstract:Interferometric synthetic aperture radar (InSAR) images reveal deformation around northern Hejin, Shanxi Province. The small baseline subset (SBAS) approach for InSAR-derived deformation indicates that the observed deformation pattern can be characterized by the sum of two phenomena: background subsidence from December 2003 to February 2009 with a cumulative displacement of approximately 5 cm and uplift from February 2009 to November 2010 with a cumulative displacement of approximately 2.5 cm. Deformation modeling indicates that the local deformation was caused by the closing and opening of a sill beneath northern Hejin. The modeled sill which is approximately 5 km long, 2 km wide, is centered at 1.5 km depth. The deformation was caused by the withdrawal and influx of subsurface water.

Key words: deformation time series; northern Hejin; SBAS-InSAR; deformation modeling; InSAR

1   Introduction

Crustal deformation can be caused by seismicity, tectonics, or anthropogenic activities. Therefore, crustal deformation monitoring can play an important role in learning more about these processes. However, traditional measurements (eg, leveling, GPS) do not provide high spatial or temporal resolution due to their inherent limitations. Currently, space-borne interferometric synthetic aperture radar (InSAR) is a well-known and widely used remote sensing technique of obtaining precise (sub-cm) surface deformation measurements over large areas (thousands of km^2) and with a high spatial density of measurements (hundreds per km^2). It has been successfully used for mapping seismic and volcanic deformations[1,2], as well as anthropogenic deformations caused by mining and oil/gas or groundw-

ater extraction[3].

Linfen Basin is a tectonically active area. Two historical earthquakes with magnitudes greater than 8.0 have occurred in Linfen Basin. The Luoyunshan Fault is located at the western boundary of Linfen Basin (Fig. 1), and northern Hejin is situated at the southern part of the Luoyunshan Fault. Initially, we generated interferograms to detect deformation around the Luoyunshan Fault. Subsequently, we found that northern Hejin shows deformation anomalies. In this study, we determined the spatial coverage and temporal evolution of the deformation of northern Hejin.

2   InSAR data and analysis

We processed all available radar data acquired by the Envisat satellite from a descending orbital track, operating at a wavelength of 56.3 mm. The data are from 2003 through 2010, with no data acquired in 2007 or 2008. We used the two-pass InSAR approach[4] to form 18 deformation interferograms with reasonably good coherence. A digital elevation model (DEM) from the Shuttle
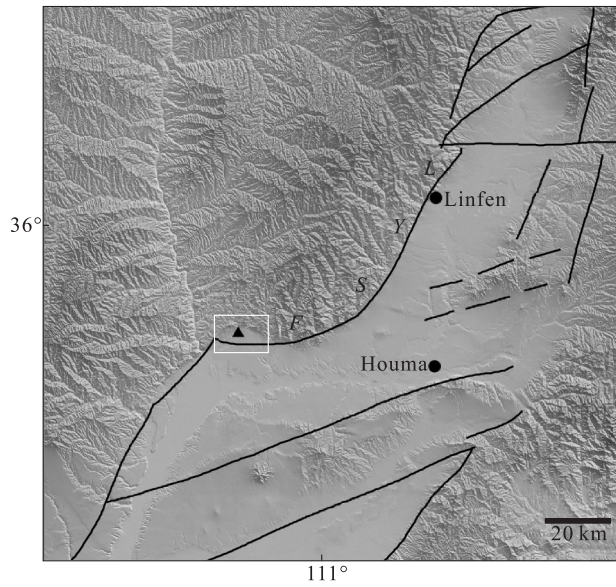
Figure 1   Shaded relief map of the area of the Hejin anomaly (The black lines represent local faults. The white box indicates the location of the interferograms shown in figures 2 and 5. The black triangle denotes the area of the deformation time series shown in Fig.4)

Radar Topography Mission (SRTM)[5] with 90-m pixel spacing was used to remove the topographic signature from the InSAR phase maps. To remove residual orbit errors, the interferogram baseline was obtained by a nonlinear least-squares adjustment of the observed phase over presumably stable areas[6]. For interferograms that were obviously contaminated by topography-correlated atmospheric delays, we made a linear correction based on topographic height, using phase observations of areas far from the volcano as a guide. Due to low coherence, interferograms were filtered twice using an adaptive filter function based on the local fringe spectrum[7], with window dimensions of 128×128 pixels for the first pass and 32×32 pixels for the second. This filtering strategy removes the high-frequency noise efficiently[8] and makes the phase unwrapping much easier.

Figure 2 shows examples of interferograms that the span time intervals is from several months to a few years. Together, these interferograms map the patterns of deformation from 2003 to 2010, leading to the following two observations:

1) Fringes that persist over time (eg, figures 2(a)-(h)) show deformation anomalies. These fringes are unlikely to be atmospheric artifacts because they were produced from independent SAR images. The signals cannot be attributed to DEM errors because the baselines of these interferograms are short, making them insensitive to any plausible errors in the DEM.
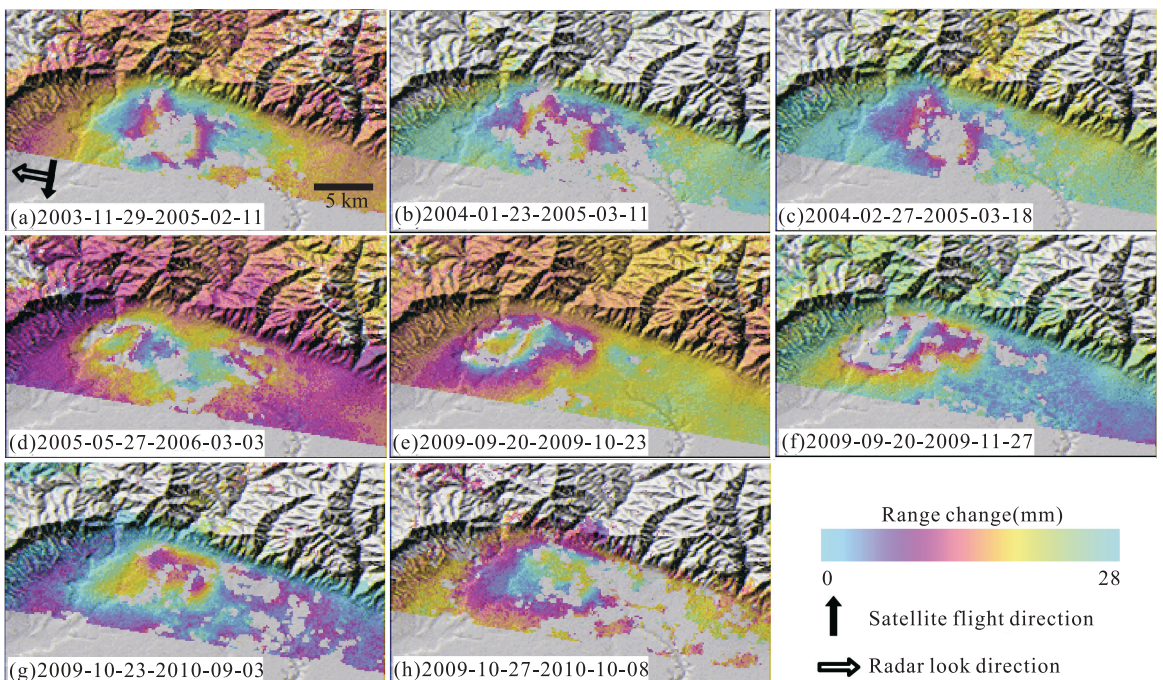

Figure 2   Interferograms labeled by period (date format is yy-mm-dd, the satellite flight and radar look directions are labeled in (a). Each fringe (full color cycle) represents 28 mm of range change between the ground and satellite. Areas that lack interferometric coherence are uncolored)

2) The deformation patterns are different during the periods between 2003-2006 (Figs. 2 (a)-(d)) and 2009-2010 (Figs. 2 (e)-(h)). Specifically, during 2003-2006, the maximum line-of-sight (LOS) increased by approximately 5 cm in an area approximately 8 km in diameter (Figs.2(a)-(d)). However, the interferograms show a maximum LOS shortening of approximately 3 cm during 2009-2010 (Figs.2(e)-(h)). The deformation center moved slightly westward between 2003-2006 (Figs. 2 (a)-(d)) and 2009-2010 (Figs.2(e)-(h)). To investigate the temporal evolution of the surface deformation, we used the small baseline subset (SBAS)[9-10] approach to retrieve the displacement time series. This methodology selects interferograms with small spatial baselines, solves the deformation rates between subsequent SAR acquisitions, and reconstructs cumulative displacements by integration. The advantage of this approach is that it can produce nonlinear time series of deformation over a long period of time using interferograms with short time spans, which are usually more coherent[11]. We selected image pairs with perpendicular baselines smaller than 400 m. Accordingly, 19 interferograms were produced, all of which were within one subset, as indicated by the connected lines in figure 3. Figure 4 shows the deformation time series of the area of maximum deformation derived by the SBAS approach (see Fig.1 for the location of this area). This is crucial information for the analysis of dynamic deformation phenomena. Figure 4 shows that the deformation pattern is characterized by the combination of two different effects: background subsidence from December 2003 through February 2009 with a cumulative displacement of approximately 5 cm and an uplift phase from February 2009 to November 2010 with a cumulative displacement of approximately 2.5 cm.

3   Deformation modeling

We assume that the deformation was caused by a volume change beneath northern Hejin. To explain the InSAR-derived deformation field, we tested a uniformly opening sill (i.e., crack) embedded in an elastic half-space[12] to model the individual interferograms with reasonably good coherence. Eight parameters define the
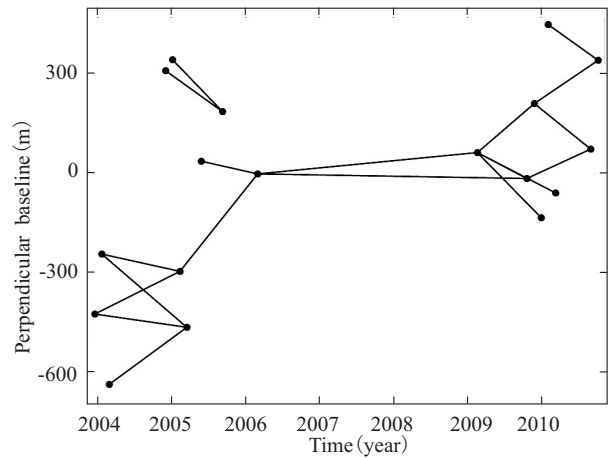

Figure 3   Baselines and InSAR combinations (Images are denoted by solid circles, and solid black lines connecting circles represent perpendicular baselines of the corresponding interferograms)
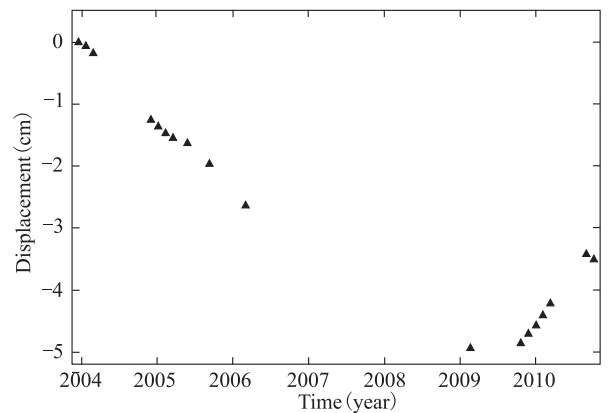

Figure 4   InSAR LOS deformation time series for the area marked by the black triangle in figure 1

sill: length, width, depth, strike, dip, opening, and location (two parameters). We introduced linear terms to the model to account for any possible phase ramp due to uncertainties in satellite positions[4]. We used the downhill simplex method and Monte Carlo simulations[13] to estimate the optimal parameters and their uncertainties, and the root mean square errors (RMSE) between the observed and modeled interferograms as the goodness-of-fit criterion. Figure 5 shows two examples, with observed (a), (d), modeled (b), (e), and residual (c), (f) interferograms for the sill models which show the differences between the observed and the modeled interferograms. The models fit each of the observed interferograms reasonably well. Due to subsidence and uplift, which may be caused by different mechanisms, we calculated the parameters of
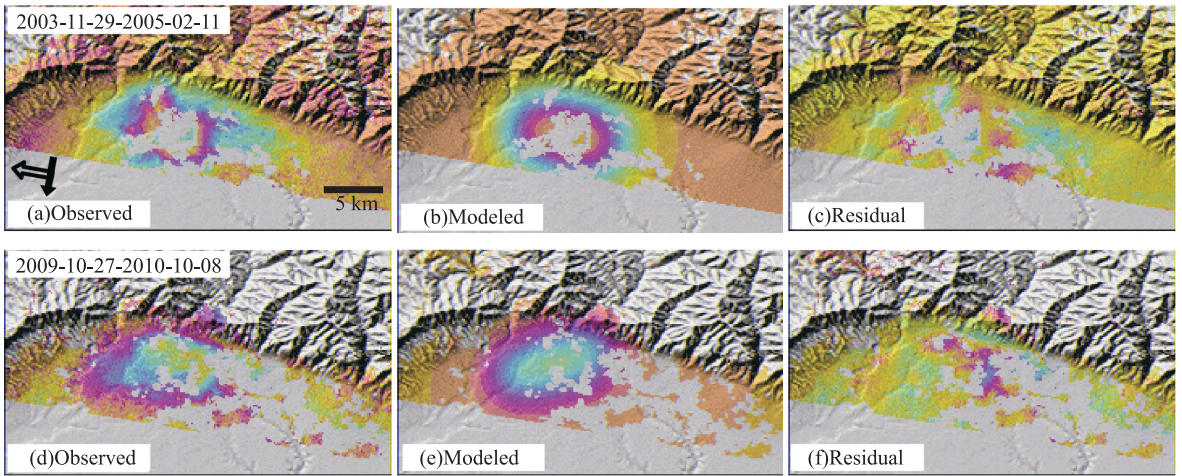
Figure 5   Two examples for the sill models

the sill models for seven deflationary and four inflationary interferograms separately. In other words, we determined the parameters of the two sill models (Tab.1) by averaging the results for seven deflationary and four inflationary interferograms separately. This strategy provides a first-order approach to reducing modeling errors. The model parameters are well constrained based on their uncertainties, as shown in table 1, which we attribute to the averaging of many interferograms. The best-fit modeled sill for the deflationary interferograms is 5.2 km long, 2.5 km wide, at 1.5 km depth, and with a strike of N104°E. The best-fit modeled sill for the inflationary interferograms is 5.4 km long, 1.6 km wide, at 1.4 km depth, and with a strike of N78°E.

Table 1   Parameters for the best-fitting modeled sill. Uncertainties correspond to 95% confidence

Parameters	Deflation	Inflation
Length(km)	5.2±0.9	5.4±0.5
Width(km)	2.5±0.4	1.6±0.2
Depth(km)	1.5±0.5	1.4±0.3
Strike(°)	104.1±1.4	78.3±8.7
X(km)	7.7±0.3	7.0±1.0
Y(km)	3.7±0.3	4.7±0.1
Open(mm)	−34.5±14.5	38.6±9.8

4   Discussion

The differences in the locations of the deflationary and inflationary sill sources are not significant at the 95% confidence level (Tab.1), so we attribute both processes to the same source. The dimensions of the two sill models are also similar, thus supporting a single source.

We speculate that the deformation was caused by the withdrawal and influx of groundwater water for three main reasons. First, no active faults or volcanoes are located in northern Hejin. Second, the deformation seems unlikely to be caused by tectonic motion based on the interferogram patterns (Fig.2). Third, the high-resolution remote sensing images indicate that the ground surface is mainly covered by crops. We speculate that the groundwater water was over-extracted during 2003-2009. After 2009, the local residents stopped extracting groundwater excessively, and the groundwater beneath northern Hejin recharged, which caused the ground to rebound, i.e., change from subsidence to uplift.

5   Conclusion

Using C-band Envisat ASAR images, we mapped the surface deformation that occurred in northern Hejin, Shanxi Province, from December 2003 to November 2010. The SBAS-InSAR-derived deformation indicates that the deformation pattern is characterized by the succession of two different processes: background subsidence from December 2003 to February 2009 with a cumulative displacement of approximately 5 cm and an uplift phase from February 2009 to November 2010 with a cumulative displacement of approximately 2.5 cm. Deformation modeling suggests that the emplace-

ment of a sill was responsible for the observed deformation, which was caused by the withdrawal and influx of groundwater.

InSAR observations from this study provide a glimpse of local deformation associated with sill closing and opening events. This study provides valuable information as a contribution to the understanding of seismic hazards and regional tectonics in this and other similar regions.

Acknowledgements

References

[1]   Simons M, Fialko Y and Rivera L. Coseismic deformation from the 1999 *M*w 7.1 Hector Mine, California, earthquake as inferred from InSAR and GPS observations. Bulletin of the Seismological Society of America, 2002, 92(4): 1390-1402.

[2]   Lu Z, Dzurisin D, Biggs J, Wicks J C and McNutt S. Ground surface deformation patterns, magma supply, and magma storage at Okmok volcano, Alaska, from InSAR analysis: 1. Intereruption deformation, 1997-2008. J Geophys Res., 2010, 115, B00B02.

[3]   Samsonov S, d'Oreye N and Smets B. Ground deformation associated with post-mining activity at the French-German border revealed by novel InSAR time series method. International Journal of Applied Earth Observation and Geoinformation, 2013, 23: 142-154.

[4]   Massonnet D and Feigl K. Radar interferometry and its application to changes in the Earth's surface. Rev Geophys., 1998, 36: 441-500.

[5]   Farr T G and Kobrick M. Shuttle radar topography mission produces a wealth of data, Eos Trans AGU., 2000, 81(48): 583-585.

[6]   Rosen P, Hensley S, Zebker H, Webb F H and Fielding E J. Surface deformation and coherence measurements of Kilauea volcano, Hawaii, from SIR-C radar interferometry, J Geophys Res., 1996, 101:23109-23125.

[7]   Goldstein R M and Werner C L. Radar interferogram filtering for geophysical applications, Geophys Res Lett., 1998, 25(21), 4035-4038, doi:10.1029/1998GL900033.

[8]   Nof R N, Ziv A, Doin M P, Baer G, Fialko Y, Wdowinski S, Eyal Y and Bock Y. Rising of the lowest place on Earth due to Dead Sea water-level drop: Evidence from SAR interferometry and GPS. J Geophys Res., 2012, 117, B05412, doi:10.1029/2011JB008961.

[9]   Berardino P, Fornaro G, Lanari R and Sansosti E. A new algorithm for surface deformation monitoring based on small baseline differential SAR interferograms. Institute of Electrical and Electronics Engineers Transactions on Geosciences and Remote Sensing, 2002, 40(11): 2375-2383.

[10]   Jung H S, Lee C W, Park J W, Kim K D and Won J S. Improvement of small baseline subset (SBAS) algorithm for measuring time-series surface deformations from differential SAR interferograms. Korean Journal of Remote Sensing, 2008, 24, 165-177. (in Korean)

[11]   Samsonov S, van der Kooij M and Tiampo K. A simultaneous inversion for deformation rates and topographic errors of DInSAR data utilizing linear least square inversion technique. Computers & Geosciences, 2011, 37(8): 1083-1091.

[12]   Okada Y. Surface deformation due to shear and tensile faults in a half-space. Bulletin Seismological Society of America 1985, 75: 1135-1154.

[13]   Press W, Teukolsky S, Vetterling W and Flannery B. Numerical recipes in C, The Art of Scientific Computing. Cambridge Univ. Press, New York, 1992, 994.